

## Article

# Amorphous Carbon Films with Embedded Well-Dispersed Nanodiamonds: Plasmon-Enhanced Analysis and Possible Antimicrobial Applications

Oleg Streletskiy <sup>1</sup>, Elena Perevedentseva <sup>2</sup>, Ilya Zavidovskiy <sup>1,\*</sup>, Artashes Karmenyan <sup>3</sup>, Vladimir Sychev <sup>2</sup>, Vera Sadykova <sup>4</sup>, Anastasia Kuvarina <sup>4</sup> and Chia-Liang Cheng <sup>3</sup>

<sup>1</sup> Faculty of Physics, M.V. Lomonosov Moscow State University, Moscow 119991, Russia

<sup>2</sup> P. N. Lebedev Physical Institute of the Russian Academy of Sciences, Moscow 119991, Russia

<sup>3</sup> Department of Physics, National Dong Hwa University, Hualien 97401, Taiwan

<sup>4</sup> Laboratory of Taxonomic Study and Collection of Cultures of Microorganisms, Gause Institute of New Antibiotics, Moscow 119021, Russia

\* Correspondence: ia.zavidovskii@physics.msu.ru

**Abstract:** An amorphous carbon film with embedded detonation nanodiamond (DND) particles (a-C:ND) was produced by magnetron sputtering of nanodiamond powder. An Ag film was deposited on the carbon structure by radiofrequency magnetron sputtering. The silver film was irradiated with a 150 eV Ar<sup>+</sup> to form plasmonic-active nanoparticles (NP) on the surface of the a-C:ND. The structure of the obtained a-C:ND and a-C:ND/Ag structures were studied by scanning and transmission electron microscopy, electron energy-loss spectroscopy, UV-Visible absorption spectroscopy, Raman spectroscopy, and fluorescence lifetime imaging at two-photon excitation. The analysis revealed 76% of sp<sup>3</sup>-carbon and a good dispersion of diamond nanoparticles in the a-C. Surface-enhanced Raman scattering (SERS) was applied to investigate the a-C:ND/Ag structure, allowing for the observation of SERS from the sp<sup>2</sup>-carbon species and the absence of significant a-C:ND damage after Ar<sup>+</sup> irradiation of the Ag overlayer. A plasmonic-metal-enhanced luminescence was observed at one- and two-photon excitations, revealing a two- to five-fold intensity increase. The activity of the used DNDs was tested using the agar diffusion method and observed against the bacteria of *Bacillus subtilis*, *Staphylococcus aureus*, and *Escherichia coli* and the fungi of *Aspergillus niger*, *Aspergillus fumigatus*, and the yeast of *Candida albicans*, showing DND activity against all the test strains of fungi.

**Keywords:** plasmonic-active silver nanoparticles; nanodiamond-based composites; microarc-assisted magnetron sputtering; surface-enhanced Raman spectroscopy of carbon species; antifungal properties of nanodiamond; fluorescence lifetime imaging at two-photon excitation; low-energy ion-beam irradiation



**Citation:** Streletskiy, O.; Perevedentseva, E.; Zavidovskiy, I.; Karmenyan, A.; Sychev, V.; Sadykova, V.; Kuvarina, A.; Cheng, C.-L. Amorphous Carbon Films with Embedded Well-Dispersed Nanodiamonds: Plasmon-Enhanced Analysis and Possible Antimicrobial Applications. *Magnetochemistry* **2022**, *8*, 171. <https://doi.org/10.3390/magnetochemistry8120171>

Academic Editors: Zhengtao Wu and Zheng Gai

Received: 2 November 2022

Accepted: 24 November 2022

Published: 26 November 2022

**Publisher's Note:** MDPI stays neutral with regard to jurisdictional claims in published maps and institutional affiliations.



**Copyright:** © 2022 by the authors. Licensee MDPI, Basel, Switzerland. This article is an open access article distributed under the terms and conditions of the Creative Commons Attribution (CC BY) license (<https://creativecommons.org/licenses/by/4.0/>).

## 1. Introduction

Nanodiamond (ND) composites are of great interest due to the versatile and tunable properties of NDs [1]. All-carbon composites usually combine coexisting carbons of sp<sup>3</sup> and sp<sup>2</sup> hybridization. In particular, one of the examples of such composites is amorphous carbon matrix with ND inclusions (a-C:ND). The sp<sup>2</sup>/amorphous carbon shell surrounding the diamond core is typical for commercially available ND particles [1,2]. This structure with a significant percentage of the sp<sup>2</sup>-sp<sup>3</sup> interface may determine the unique physicochemical properties of carbon composites (which depends also on the particle size, spatial distribution, diamond lattice defects, surface functionalization, etc.) and offers a wide range of possible applications of the resulting a-C:ND material [3]. Most of the applications of the composite require controllable NDs with pre-established surface structure and functionalization as well as particle dispersion in the matrix/film and their alignment.

Among the wide variety of nanodiamonds available, detonation NDs (DNDs) with a small (3–5 nm) diamond crystallite/core are especially attractive; however, the tight

aggregation of a DND can complicate its application, particularly for the synthesis of composites with preset properties. Significant efforts are applied to disaggregate DNDs and prepare highly dispersed DND systems. The methods to get well-dispersed colloidal systems are still the subjects of recent studies [4].

As for ND embedding into solid media, the well-dispersed distribution of DNDs is also of high interest: e.g., the monodispersed distribution of DNDs in a bulk polymer matrix is discussed in [5]. We have succeeded in synthesizing a hybrid structure with NDs well-dispersed in an amorphous carbon thin film matrix by magnetron sputtering of ND powder in a pulsed mode. The direct current sputtering of the insulating ND powder in a pulsed mode induced the formation of microarcs on a target surface. The microarcing process led to the NDs charging and subsequent detachment of the charged particles from the magnetron target surface. In its turn, the Coulomb repulsion of the charged NDs during their transfer to the substrate resulted in the dispersion of detonation nanodiamond particles embedded into the  $sp^3$ -rich amorphous carbon film. As a result, a-C:ND coatings with uniformly distributed DND inclusions were produced by using magnetron sputtering of nanodiamond powder [6]. This technique ensuring uniform dispersion of DND inclusions in a matrix may be beneficial for a number of applications. Thus, the possibility of creating thin homogeneous layers of a well-dispersed ND with a predictable, controlled, and reproducible structure with photoluminescence originating from the color centers is of particular interest for application in the fields of quantum technologies, secure quantum communication, quantum information processing [7], and in the semiconductor industry as a whole [8]. It may be also useful in sensing and biosensing methods and the development of new devices [9], e.g., for chemical [9,10], thermo- [11], magnetic sensing [12] and molecular and biosensing [13–15]. As fluorescence lifetime imaging (FLIM) has been successfully applied for the study of NDs [16,17], the analysis of the structures capable of ND luminescence-based sensing is of particular interest. As for the a-C:ND films, the variability of carbon matrix properties also gives rise to the study of various applications of such structures [18–27], particularly, as reinforcement coatings [20–23].

Due to their biocompatibility, a-C:ND films are also of interest for biomedical coatings aimed at enhancing cellular growth for bone and tissue repair [24,25]. Being biocompatible with animal cells and tissues, a-C and ND-based films show activity against some bacteria and other microorganisms; therefore, such structures may become a basis of novel coatings for medical devices, implants, etc. [26,27]. Therefore, synthesizing all-carbon hybrid material with preset properties (structure, ordering, presence of surface functional groups, color centers, etc.) as well as methods of characterizing the composite material are topical tasks.

In the current work, the morphology and structure of the obtained a-C:ND/Ag hybrid were observed by means of scanning and transmission electron microscopy (SEM, TEM), electron energy-loss spectroscopy (EELS), Raman spectroscopy, and two-photon fluorescence lifetime microscopy (TP-FLIM). For the structure analysis, SERS-active nanostructured silver was deposited on the a-C:ND composite by radio-frequency magnetron sputtering of the Ag target, followed by low-energy ion irradiation [28]. The ion-beam treatment method induced the sputtering and surface diffusion of the silver, which lead to the formation of SERS-active nanoparticles [29]. SERS induced by the interaction of a-C:ND and AgNP was applied to analyze the local structural peculiarities of the amorphous carbon matrix and the surface of the composite films formed. The SERS technique had previously been found to be sensitive to the  $sp^2$ -hybridized fraction of carbon structures [30–32]. Besides the enhanced Raman signal, plasmon-enhanced luminescence was observed. Its origin was discussed based on spectroscopic measurements and the analysis of the spatial distribution of emitters and their luminescence lifetimes by means of FLIM. The reported analysis methods are of interest for the study of the structure and properties of nanostructured carbon systems as well as for the investigation of the media surrounding nanoparticles in a-C:ND structures.

As an example of the expected applications of a-C:ND, in this paper, we discuss the preparation of antimicrobial coatings. The uniform dispersion of DND inclusions in the matrix may also ensure utilizing DND antibacterial potential for the development of a new antibacterial coating. To discuss this perspective, the antimicrobial activity of the DND component of the a-C:ND structure was tested against a number of pathogenic gram-positive and gram-negative bacteria and fungi.

## 2. Materials and Methods

### 2.1. Target Manufacturing

The sputtering target was prepared from a DND powder (FRPC “Altai”, Russia) and a standard MPG-7 graphite magnetron target (Grafi, Russia). The suspension of the DND powder was stirred in acetone, uniformly planted on the graphite target, and dried under ambient conditions. The thickness of the DND layer on the target surface estimated by the mass of the diluted DND powder was approximately 10  $\mu\text{m}$ . The significant thickness of the DND layer was set up to prevent graphite target sputtering and guarantee the determining of the properties of the films by the processes taking place during the interaction between the DND layer and the magnetron discharge. The precursor DND powder had been characterized in detail previously [6]. The average DND particle size was 5 nm [6].

### 2.2. Deposition Stages

The deposition of the a-C:ND/Ag structure included the following steps: (1) manufacturing of target containing detonation nanodiamond (DND), which was discussed in Section 2.1; (2) a-C:ND film synthesis by magnetron sputtering of the DND-based target in a pulsed mode; (3) radio-frequency (RF) magnetron sputtering of Ag film; (4) Ag film post-deposition treatment by  $\text{Ar}^+$  ion beam resulting in Ag nanoparticle formation. Step 2 is shown schematically in Figure 1. The structure deposition and modification of Steps 2–4 is depicted in Figure 2.

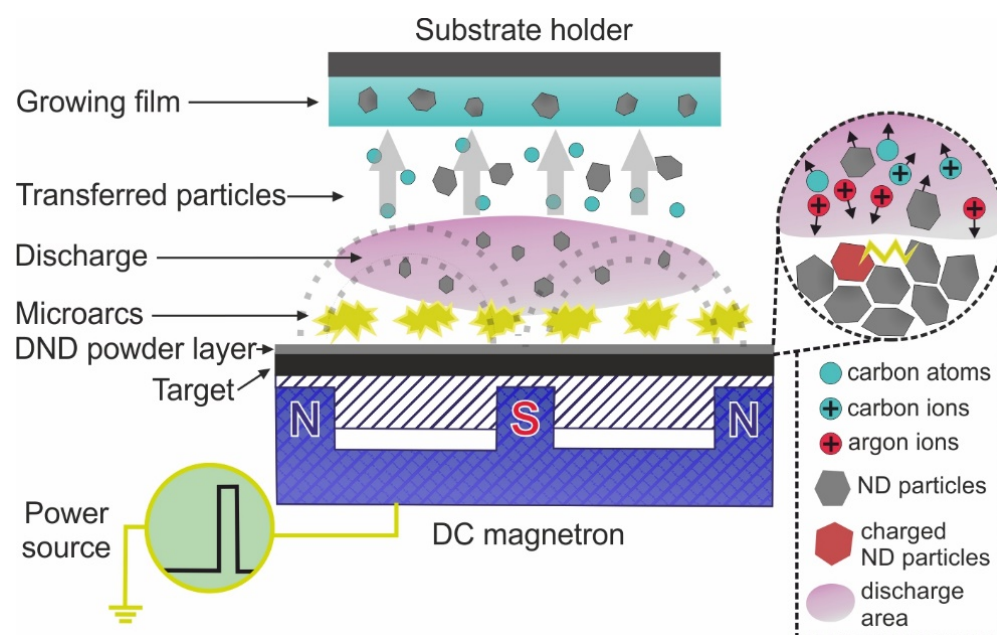


**Figure 1.** Schematic of the synthesis of a-C:ND coatings in a pulsed mode of DC magnetron sputtering. The microarcing process leading to the ND transfer from the target to the substrate is shown in the inset.

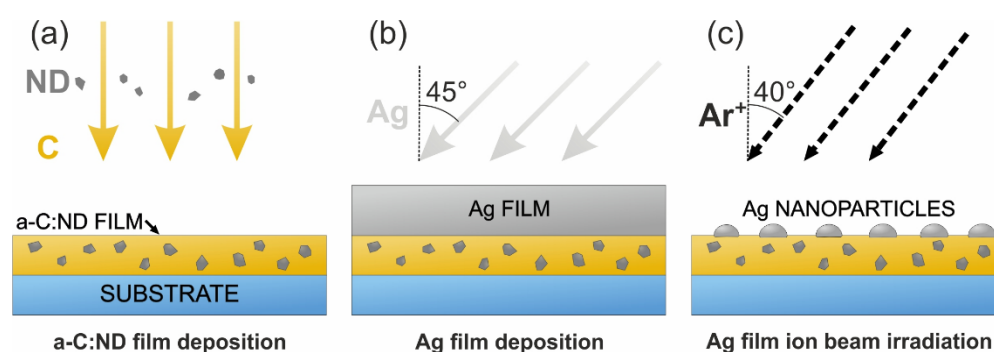


**Figure 2.** Formation and modification of a-C:ND/Ag structure (steps 2–4). (a) a-C:ND film deposition by magnetron sputtering in a pulsed mode (step 2). (b) Deposition of the silver film by RF magnetron sputtering of the Ag target (step 3). (c) Ion-beam treatment of the Ag film resulting in the formation of the nanoparticles (step 4).

The investigated a-C:ND films were synthesized during the second step by means of direct current (DC) magnetron sputtering of the graphite target covered with a 10  $\mu\text{m}$  layer of DND in a pulsed mode (Figures 1 and 2a). The deposition was carried out in a high vacuum chamber and pumped to the residual pressure of  $10^{-4}$  Pa. The ion-beam etching of the substrates and deposition were carried out at an argon pressure of  $10^{-1}$  Pa. The discharge voltage was 500 V, the pulse duration  $\sim 0.5$  s, the pulse frequency  $\sim 1$  Hz, and the pulse number was equal to 10. The charge accumulation on the insulating DND layer during the deposition induced local electric breakdowns or microarcs. A large number of microarcs were formed on the DND layer during the deposition. Microarcing also led to the effective transfer of the nanodiamonds from the target [6]. Unlike other techniques of ND-based target sputtering, microarcing “de-localizes” the interaction between the target and the plasma, thus reducing the graphitization of the NDs [6]. The spacing between the target and the substrate holder was  $\sim 15$  cm. The thickness of the deposited coatings estimated by transmission electron microscopy (TEM) of the edges of folded films was 15 nm. Cover glass, polished Si, and freshly cleaved NaCl monocrystal were used as substrates. Before the deposition, the substrate surfaces were cleaned for 5 min by normally incident 1000 eV  $\text{Ar}^+$  ion beam. The ion beam was produced via a Hall ion-beam source with a cold hollow cathode Klan 53-M (Platar Corp., Moscow, Russia). The temperature of the substrates measured by the thermocouple located inside the substrate holder did not exceed 300 K during the deposition process.

### 2.3. SERS-Active Media Formation

The deposition of Ag nanoparticles was carried out to investigate the a-C:ND coatings by SERS technique and plasmon-enhanced luminescence spectroscopy. The process included 2 steps (steps 3 and 4). First, a silver polycrystalline film was deposited on top of a-C:ND coating by RF magnetron sputtering of the 30 W power at the  $10^{-1}$  Pa pressure in Ar atmosphere (Figure 2b). The angle between the particle flux and the substrate surface was  $45^\circ$ . Thickness of the deposited film monitored by a quartz-crystal sensor was  $\sim 25$  nm. Then, the grown film was irradiated with the 150 eV  $\text{Ar}^+$  ions and  $5 \times 10^{16}$  ion/cm<sup>2</sup> dose (Figure 2c). The angle of  $40^\circ$  was set between the ion-beam axis and the normal to the substrate surface. The film thickness and irradiation dose were chosen in accordance with [29], as these deposition parameters ensure low damage to the underlying layer and sufficient SERS effect.

### 2.4. Structural Investigations

High-resolution transmission electron microscopic (HRTEM) investigations were performed by the JEM 2100F microscope (JEOL, Tokyo, Japan) at the 200 kV accelerating voltage. The samples were prepared for TEM by dissolving a NaCl substrate in distilled water and subsequently placing the floating film on the grid.

Electron energy loss (EELS) carbon pre-K edge spectra were detected with the TEM module based on the Omega energy filter.

UV-Visible absorption (UV-Vis) spectra were obtained by the Unico-2802 spectrophotometer (Unico LLC, Seattle, WA, USA). In the spectrophotometer setup, the solution cuvette has been replaced with a holder of cover glasses for transmittance measurements.

Scanning electron microscopy (SEM) images were obtained by the SEM JSM6500F (JEOL, Tokyo, Japan).

The statistical analysis of the images was carried out via Gwyddion software (Gwyddion 2.61, open-source software, Brno, Czech Republic, <http://gwyddion.net/>, accessed on 25 October 2022). The average distance between the particles was estimated as a square root of the area per particle.

The spectra were measured using Raman microspectrometers: Renishaw1000 (Renishaw, Wotton-under-Edge, GB) equipped with a 532 nm solid-state continuous wave (CW) DPSS laser (Coherent Inc., Santa Clara, CA, USA), a grid 1800 1/mm, microscope, and an objective N Plan  $\times 50/0.75$  (Leica, Wetzlar, Germany). The spectra were measured with the laser power of  $\sim 15$  mW in a focal spot, 10 s acquisition time (Raman, SERS), and  $10 \times 10$  s for Raman and photoluminescence (PL).

TP-FLIM was used to visualize the film structure via two-photon excited luminescence of nanodiamond particles embedded into a-C matrix and to analyze the luminescence lifetimes. A tunable Ti-sapphire laser (Chameleon Ultra-II, Coherent, USA) was used for the two-photon excitation; the wavelength was 780 nm, the pulse duration was 140 fs, and the repetition rate was 80 MHz. The FLIM was performed with a 2D scanner (EINST Technology, Singapore) coupled with the Olympus IX 71 inverted microscope. The objective UPlanFLN  $\times 40/0.75$  (Olympus, Tokyo, Japan) was used. The signal registration in the spectral range of 450–640 nm was done by means of a PicoHarp 300 (PicoQuant GmbH, Berlin, Germany) single photon counting system and thermoelectrically cooled PMT. The FLIM data were analyzed using the commercially available software SymPho Time (PicoQuant GmbH, Berlin, Germany).

### 2.5. Estimation of DND Antimicrobial and Antifungal Activity

The antimicrobial activity of ultradispersed ND was assessed by the agar diffusion method [33]. All samples were tested at the concentration of 500  $\mu\text{g}/\text{mL}$ . Inhibition zones were measured manually using a digital caliper. Assays were performed three times in triplicate. Amphotericin B 40  $\mu\text{g}$  («NII Pasteur», Saint Petersburg, Russia), nystatin 80  $\mu\text{g}$  («NII Pasteur», Russia), and amoxiclav 10  $\mu\text{g}$  («NII Pasteur», Saint Petersburg, Russia) were used as positive controls. The antibacterial activity was assessed with the following test strains: gram-negative bacteria of *Escherichia coli* ATCC 25922 and *Pseudomonas aeruginosa* ATCC 27853; gram-positive bacteria *Bacillus subtilis* ATCC 6633; and *Staphylococcus aureus* 209P and *Micrococcus luteus* NCTC 8340. The antifungal activity was assessed with the following test strains: the fungi of the genus *Aspergillus*—*A. niger* INA 00760, *A. fumigatus* KPB F-37, and the yeast of *Candida albicans* ATCC 2091.

The test culture of *B. subtilis* ATCC 6633 was grown on the Gause 2 medium (g/L): 2.5 tryptone (or 30 mL Hottinger broth), peptone-5, sodium chloride-5, and glucose-10. *S. aureus* 209P, *M. luteus* NCTC 8340, and *P. aeruginosa* ATCC 27853 were grown on the MPA (meat peptone agar) medium, and *E. coli* ATCC 25922 was grown on the LB (tryptone soy agar).

## 3. Results and Discussion

### 3.1. Characterization of a-C:ND Coating

#### 3.1.1. SEM

The SEM image of the a-C:ND film on Si substrate is presented in Figure 3. Well-dispersed nanosized inclusions can be observed via SEM. SEM studies were carried out at 15 kV electron accelerating voltage. To investigate the origin and structure of the inclusions, the TEM analysis of the samples was carried out.

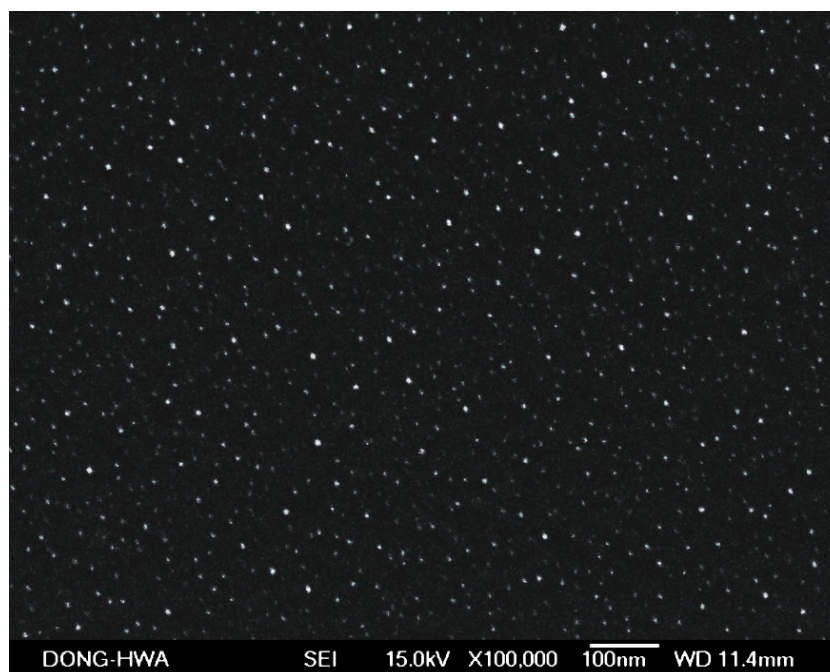


**Figure 3.** SEM image of a-C:ND film on Si.

### 3.1.2. HRTEM

The TEM image of the a-C:ND structure, the distribution of the nanoparticle sizes, the HRTEM, and the Fast Fourier Transform (FFT) of the HRTEM image of an individual nanoparticle are shown in Figure 4. TEM and EELS studies were carried out at 200 kV electron accelerating voltage. The HRTEM (Figure 4c) confirms the previously discussed results [6], verifying that microarc-assisted sputtering of NDs resulted in the transfer of separate monocrystalline nanoparticles from the magnetron target to the surface of the growing film. However, as magnetron sputtering also led to the condensation of the vapor of the carbon atoms on the growing film surface; the resulting structure was the NDs incorporated into the amorphous carbon matrix (a-C:ND), which can be observed from the overview of the structure (Figure 4b). The average size and average distance between the centers of the nanoparticles embedded into the a-C matrix were  $\sim 4$  nm and  $\sim 29$  nm, respectively, corresponding to the  $1190 \mu\text{m}^{-2}$  aerial density of the nanoparticles (Figure 4a,b). The FFT images obtained for individual particles correspond to the structure of a cubic diamond lattice; the characteristic FFT image of an individual particle is shown in Figure 4d. The analysis of the FFT image of the individual inclusion showed that its point reflexes corresponded to the  $2.06 \pm 0.02 \text{ \AA}$  interplanar spacing. Such a value is in good agreement with the value typical for the (111) plane of cubic diamond [34]. This proved that monocrystalline NDs were transferred from the substrate surface with only slight damage during the deposition process. In addition, as the ND particles became charged during the sputtering process, they exhibited Coulomb repulsion during the transfer, resulting in the uniform dispersion of the monocrystalline NDs in the matrix of the amorphous carbon. However, the applied method of achieving well-dispersed NDs requires no more than 10 magnetron pulses. A higher number of magnetron pulses leads to the graphitization and agglomeration of the particles, limiting the obtainable thickness of the coatings [6].

### 3.1.3. EELS

The estimation of the ratio of the  $sp^3$ -hybridized atoms was carried out by three-Gaussian spectra fitting of EELS carbon pre-K edge spectra [35] after the subtraction of the Tougaard baseline. The two peaks (Figure 5) observed in this range are attributed to the  $1s \rightarrow \pi^*$  and  $1s \rightarrow \sigma^*$  electron interband transitions inducing the characteristic energy losses of the primary electron beam. As the  $\pi^*$ -sub-band is assigned to the presence of

the  $sp^2$ -hybridized atoms, the “ $1s \rightarrow \pi^*$ ” to “ $1s \rightarrow \sigma^*$ ” intensity ratio provides information about the ratio between  $sp^2$ - and  $sp^3$ -carbon. However, as discussed in [6], the estimation of the  $sp^2/sp^3$  ratio is interfered with by the contribution of heteroatom-induced interband transitions and fitting arbitrariness.

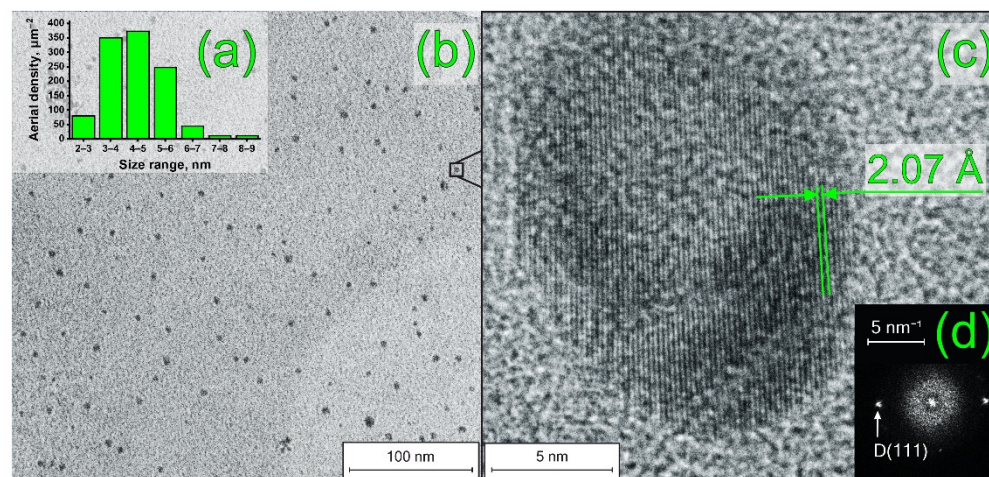


**Figure 4.** (a) Nanoparticles size distribution; (b) overview TEM image; (c) HRTEM image of the individual particle and its characteristic interplanar distance; (d) FFT of the HRTEM image of the encapsulated ND.

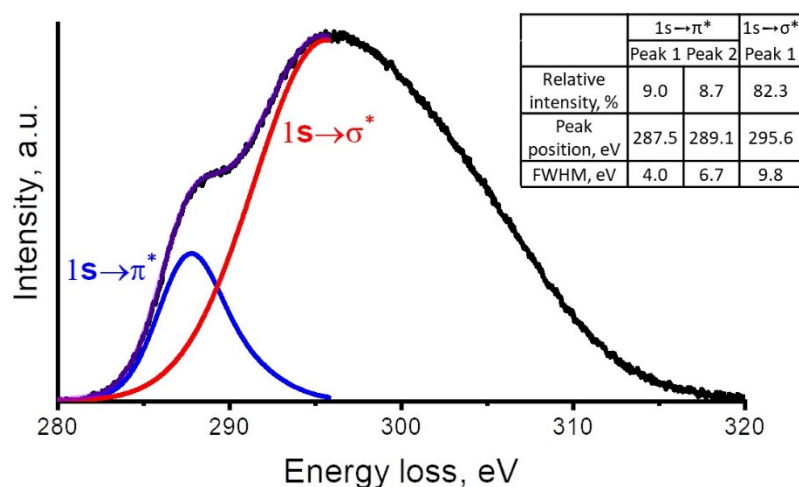


**Figure 5.** EELS spectrum of the a-C:ND sample. The contribution of the “ $1s \rightarrow \pi^*$ ” and the “ $1s \rightarrow \sigma^*$ ” lines is shown by blue and red lines, respectively; their cumulative intensity is indicated by a purple line; black line shows the experimental data. The fitting parameters are presented in the inset.

This estimated fraction of the  $sp^3$ -hybridized carbon atoms was  $76 \pm 8\%$ . The presence of  $sp^2$ -hybridized atoms corresponds to the amorphous carbon matrix surrounding diamond nanoparticles and the surface of the NDs graphitized by ion irradiation over the course of magnetron sputtering and microarcing.

### 3.2. Ag Nanoparticles Characterization

#### 3.2.1. SEM

The SEM image of the Ag nanoparticles on the a-C:ND film formed after post-deposition  $Ar^+$  ion irradiation is shown in Figure 6. SEM studies were carried out at a 15 kV electron accelerating voltage. The statistical analysis of the size distribution of the Ag particles obtained from the processing of the SEM images is shown in the inset of Figure 6. According to this data, the size of the particles was  $18 \pm 6$  nm, with the

average distance between the nanoparticles being 37 nm, corresponding to the  $730 \mu\text{m}^{-2}$  aerial density.

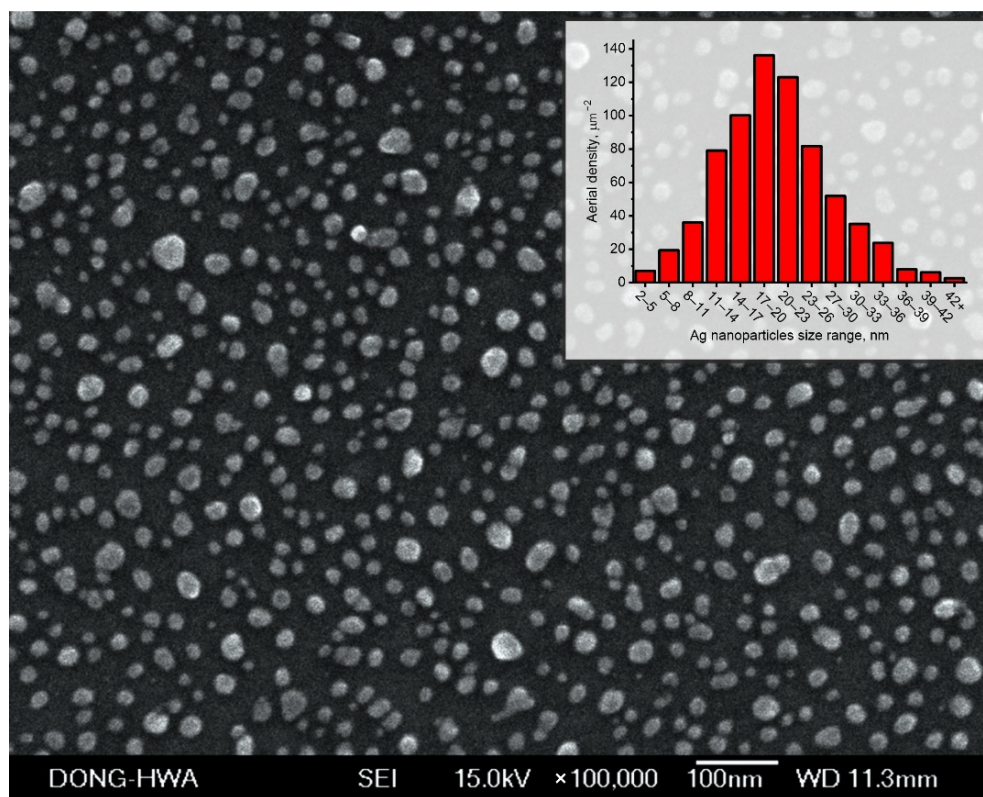


**Figure 6.** SEM image of the silver nanoparticles of a-C:ND/Ag; size distribution of silver nanoparticles is shown in the inset.

The formation of the SERS-active Ag nanoparticles by low-energy (150 eV) ion irradiation is of recent interest [28,36], as higher ion energies usually cause ion-beam mixing or amorphization of the structure [36–39]. We should also note that 150 eV  $\text{Ar}^+$  ions modify only the subsurface layer of the materials [40]. Therefore, the a-C:ND film located below the silver NP is not affected by the ion beam, while the unshaded carbon structure is only slightly damaged. Thus, the low-energy ion irradiation of the a-C:ND/Ag structure aimed at the enhancement of the Raman signal from carbon composite causes no significant deterioration of the analyzed structure. Additionally, the routes of the synthesis of AgNP not involving harmful chemical substances are widely investigated nowadays, as they are less harmful to the environment [41].

The main highlight of the applied ion-beam treatment method is an ion channeling-induced rearrangement of silver resulting in the single-crystalline structure of the AgNP [42]. Monocrystallinity ensures the excellent stability of the silver nanoparticles to oxidation and sulfidation [43]. Aside from this, the sufficient thickness of the initial film ensures that the effect of a low-energy ion beam on the subsurface layers of the carbon structure is insignificant [29]. Therefore, the application of the suggested technique to the analysis of a-C:ND all-carbon material has great diagnostic potential. We should also note that Ag deposition can increase the applicability of the studied structure, allowing for the investigation of the interaction of a-C:ND and AgNP with bacteria by using a silver substructure as a SERS-active agent. In the present work, SERS was used to analyze the local structural peculiarities of an amorphous carbon matrix and the surface of the composite films formed in the process of the condensation of NDs and sputtered carbon atoms.

### 3.2.2. UV–Vis Absorbance Spectra

The UV–Visible absorbance spectrum of Ag nanoparticles deposited on the cover glass is shown in Figure 7. It depicts the localized surface plasmon resonance (LSPR) maximum at 414 nm, which is typical for 20 nm nanoparticles [44]. However, according to Mie theory, single dipole per particle approximation, and modified long-wavelength approximation, the LSPR position for an individual, spherical, 20 nm particle is  $\sim 370\text{--}380$  nm [45]. As the plasmonic activity of AgNP manufactured by low-energy ion irradiation in similar conditions is considerably larger than for individual nanoparticles [29], the redshift of the observed LSPR wavelength may originate from the hotspot-related interaction between nanoparticles [46,47].

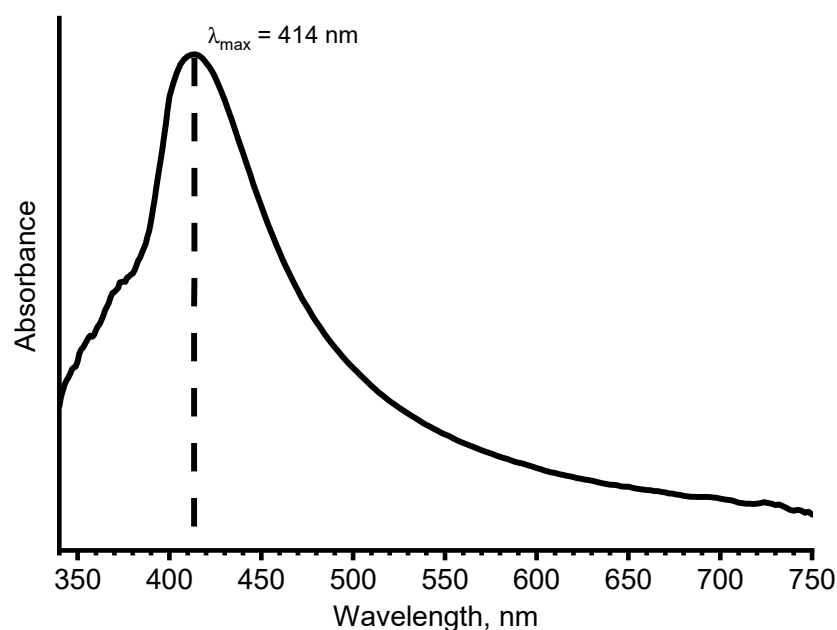


**Figure 7.** Absorbance spectrum of Ag nanoparticles.

### 3.3. Raman Spectroscopy

The Raman spectra of the prepared samples were measured at a 532 nm wavelength laser excitation. Figure 8 shows the spectra of the a-C:ND and a-C:ND/Ag samples. The Lorentzian fitting of these spectra was carried out by Origin 7 software; the fitting parameters are shown in Table 1. The spectra of the a-C:ND vary significantly at different points, revealing the shapes typical for both amorphous carbon of  $sp^2\text{--}sp^3$  hybridization (wide peaks falling into the spectral intervals  $1320\text{--}1360\text{ cm}^{-1}$  and  $1520\text{--}1600\text{ cm}^{-1}$  [48,49]) and  $sp^2$ -carbon (D-band and G-band) [48], as shown by the spectra 1-2 in Figure 8. Spectra (1) and (2) of Figure 8 demonstrate that the ratio of intensities of the D and G peaks  $I_D/I_G$  of a-C:ND film varies in a wide range. This is a result of the combination of a-C (characteristic of spectrum (1), which G-peak shifted to lower wavenumbers) and incorporated DND (spectrum (2) which is quite characteristic for DND).

The diamond peak ( $1332\text{ cm}^{-1}$ ) was not clearly observed with Raman spectroscopy, while the diamond structure was revealed via HRTEM and FFT analysis (Figure 4), which is not surprising, as the Raman cross-section of the  $sp^3$ -hybridized carbon is  $\sim 50\text{--}200$  times smaller than for the  $sp^2$ -carbon [50]. Therefore, the  $sp^2/sp^3$ -carbon shell of the NDs and matrix surrounding the nanoparticles contributed significantly to the measured spectra, considerably prevailing the contribution of the NDs' core.

The intensity of the spectra of the a-C:ND/Ag sample increased noticeably compared with the spectra of the a-C:ND (Figure 8, spectra 3-6). Additionally, the fitting of the enhanced spectrum (3) demonstrated predominantly the D and G bands of  $sp^2$ -bonded carbon. Although the plasmon resonance of the deposited Ag was in the range of  $400\text{--}450$  nm,

we can suggest that the SERS can be observed at the 532 nm excitation [44]. Therefore, Ag nanoparticles serve as an enhancing agent for carbon structures, increasing the SERS-related intensity. We should also note that the high efficiency of SERS spectroscopy in revealing the structure and physical properties of some nanocrystals, particularly, nanostructured carbon, was described in [30–32,50]. The enhancement of Raman scattering in the vicinity of noble metal nanostructures may involve both electromagnetic and chemical mechanisms. The electromagnetic mechanism takes place due to the increase of the electromagnetic field of incident light due to the excitation of localized surface plasmon near the SERS-active agent. In its turn, the chemical mechanism involves the creation of charge-transfer states between the adsorbed analyte and metal particles. For SERS-active nanostructured Ag, both mechanisms can be involved [51]. In general, SERS is observed when the excitation wavelength overlaps the plasmon resonance frequency of the SERS-active structure. However, the study of the efficiency of enhancement as a function of the characteristic size of noble metal nanostructures and excitation wavelength [44] demonstrates the acceptable efficiency of SERS for Ag nanoparticles of 20–40 nm and LSPR with a maximum near 400–450 nm at an excitation up to 532 nm. It allows using the wavelength of 532 nm for the SERS study.

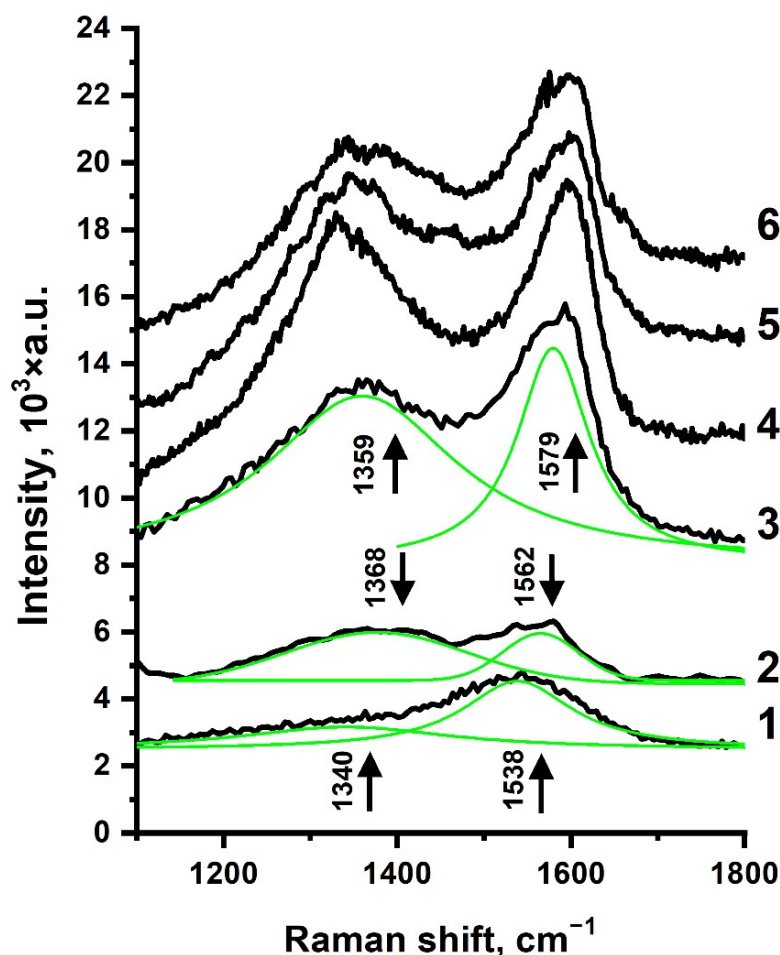


**Figure 8.** Variable Raman spectra of a-C:ND (1–2) and enhanced spectra of a-C:ND/Ag (3–6). Excitation wavelength 532 nm, laser power in a focal spot ~15 mW. Typical line positions are indicated. Black lines show the experimental data, green lines indicate its fitting with Lorentzian lines.

The enhanced spectra (Figure 8, spectra 3–6) also demonstrated some variability. In conventional Raman scattering, the G and D bands are considered the convolution of the vibrational modes related to various components of carbon structures (except diamonds). For SERS, when a structural unit (e.g., local surface defect) is in close contact with a nanostructured Ag surface, its Raman signal can be increased selectively, resulting in the

enhancement of the corresponding peaks in the spectrum [30]. The enhanced spectra showed characteristic D and G peaks. Additionally, some selected enhancements on the common background of the D and G bands can be observed, although it was not well-pronounced under the used measurement conditions. For example, one can observe the band at  $1450\text{ cm}^{-1}$  assigned as transpolyacetylene vibration [52–54], which might originate from the ion-induced decomposition of the residual hydrogen and hydrocarbons on the surface of the growing film [55]. The bands in the range of  $1518\text{--}1590\text{ cm}^{-1}$  arose from convolute graphite nanostructures. Both the frequencies and intensities of these bands depend on the curvature, the symmetry of the tube-like nanostructure, and the number of graphite layers [56,57]. The peaks observed in the range of  $1550\text{--}1560\text{ cm}^{-1}$  were related to the D-bands attributed to the amorphous phases [58] with predominant content of  $\text{sp}^2$ -carbon [48]. Thus, SERS spectra provided experimental evidence for the existence of different structural units and local defects in nanostructured carbon. As for the a-C:ND spectra variation with the AgNP formation, only a slight enhancement of the relative intensity of the D-band was observed after the deposition of Ag nanoparticles, which might originate from the minor damage of the amorphous carbon matrix induced by ion irradiation. The D-line intensity enlargement might also originate from the surface sensitivity of Raman scattering enhanced by nanostructured silver. Apparently, the surface layer was more disordered and  $\text{sp}^2$ -enriched than the bulk film, which is typical for the films deposited by ion-plasma methods [59–61]. Thus, a slight difference between the spectra of the a-C:ND and a-C:ND/Ag structures may indicate that the subsurface layers of the films were damaged insignificantly by the ion beam, which may be promising for the spectroscopic analysis of organic structures SERS-enhanced by Ag nanoparticles synthesized via the suggested low-energy irradiation technique.

**Table 1.** The parameters of the spectra fitting.  $X_c$ ,  $W$  and  $A$  are the positions, widths, and intensities of the Lorentzian peaks.  $I_D/I_G$  is a ratio of the D- and G-peak intensities.

Spectrum	D-Peak			G-Peak			$I_D/I_G$
	$X_c, \text{cm}^{-1}$	$W, \text{cm}^{-1}$	$A, 10^3 \times \text{a.u.}$	$X_c, \text{cm}^{-1}$	$W, \text{cm}^{-1}$	$A, 10^3 \times \text{a.u.}$	
1	$1340 \pm 10$	$290 \pm 28$	$294 \pm 30$	$1538 \pm 2$	$153 \pm 6$	$481 \pm 24$	$0.61 \pm 0.09$
2	$1368 \pm 3$	$271 \pm 11$	$392.5 \pm 9$	$1562 \pm 1$	$102 \pm 5$	$151 \pm 5$	$2.59 \pm 0.13$
3	$1359 \pm 2$	$268 \pm 9$	$1578 \pm 50$	$1579 \pm 1$	$101 \pm 3$	$955 \pm 34$	$1.65 \pm 0.12$

### 3.4. Photoluminescence of a-C:ND and a-C:ND/Ag

In addition to SERS, the hybrid a-C:ND/Ag samples also demonstrated enhanced luminescence compared with the a-C:ND sample. The spectrum measured at a 532 nm wavelength laser excitation revealed a SERS signal of nondiamond surface fraction on the background of luminescence whose wide peak is centered in the vicinity of 600 nm (Figure 9a). In general, luminescence in this range can be attributed to the  $\text{NV}^0$  defect color center in NDs [62]. It can be considered as a result of radiative recombination via additional energy levels in the diamond nanoparticles' band gap arising from local surface structural units or energy-trapping defects [63,64]. In addition, the contribution of the carbon-dot-like fluorescence from graphitic or amorphous carbon to this range is also possible [65]. The luminescence of nanocarbon can be modified by surface plasmons. The optimal distance between a noble metal particle and a carbon structural unit is required for luminescence amplification, similarly to the plasmon-enhanced luminescence of other kinds of fluorophores. Noble-metal-modified luminescence was reported previously for different nanocarbons. It was observed for nanodiamonds [32,66,67] as a result of local field enhancement leading to the strong modification of the local density of optical states. The enhancement of the luminescence of nanodiamonds enriched with  $\text{NV}^-$  centers (fluorescent nanodiamond, FND) attached to a silver surface was demonstrated [32,66,68,69]. In the case of FNDs, one of the main factors determining the resulting enhancement or quenching of the luminescence is the distance between the luminescence source (color center) in the

ND and the nanostructured metal surface. A separating distance of a few nm is crucial for enhancement [66]. The defect luminescent centers in NDs are embedded in the diamond core and, accordingly, separated from the metal surface by the nondiamond carbon surface layer and the diamond's environment [32,66]. Thus, the distance between some of the luminescent centers and AgNP can be optimal for PL enhancement. Note that one-photon excited PL was observed not only for nanodiamonds, but also for carbon dots interacting with plasmonic metal [70,71] and for carbon films [72].

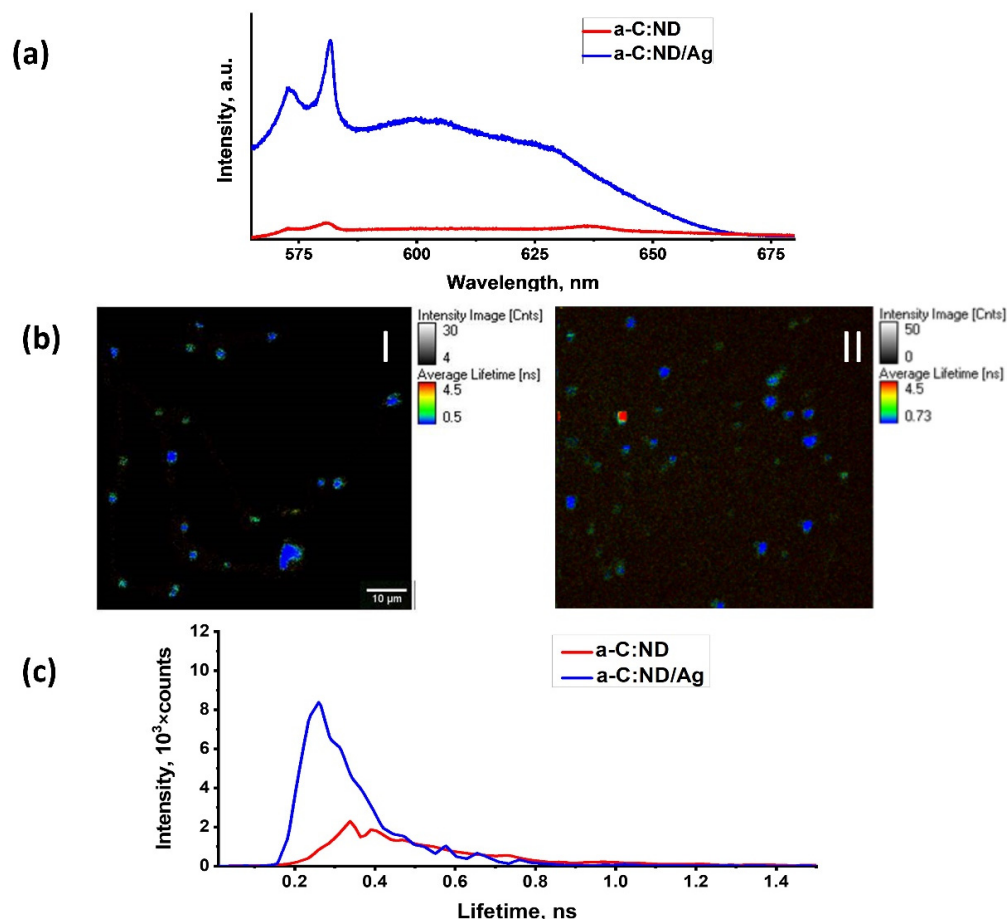


**Figure 9.** (a) PL spectra of a-C:ND and a-C:ND/Ag under the 532 nm laser excitation, laser power in a focal spot  $\sim 15$  mW; (b) TP-FLIM at the fs excitation with the 780 nm wavelength signal detection in the range of 450–640 nm: (I) FLIM image of a-C:ND, excitation power in focal spot is 4 mW; (II) FLIM image of a-C:ND/Ag, power is 1.3 mW; (c) histograms of the distribution of luminescence lifetimes of the ND embedded into a-C:ND and a-C:ND-Ag; power is 4.5 mW.

Therefore, one-photon luminescence could be excited in different carbon structures; however, the spectra shown in Figure 9a reveal a wide peak centered near 600 nm, which can indicate the contribution of an  $NV^0$  defect center PL being common enough for a phonon sideband of PL of  $NV^0$ . However, the luminescence from various defects and surface states may contribute to its line shape and intensity. More certain assignments of the source of PL in the a-C:ND film may be carried out at two-photon absorption. The two-photon excited PL in the prepared a-C:ND and a-C:ND/Ag samples was observed, visualized with FLIM, and analyzed. The FLIM of the a-C:ND (Figure 9b-I) showed a set of weakly fluorescent nanoparticles distributed in a nonfluorescent matrix. In general, the image is similar to the ND distribution in the SEM image. The two-photon luminescence (TPL) manifestation was reported for different color centers in the NDs [73]; the application of NDs and FNDs as imaging agents at two-photon excitation was discussed in [74]. Moreover, the two-photon PL was demonstrated in the case of nondiamond nanocarbons, carbon

dots, and carbon-dot-like components of surface graphitic and amorphous carbon [75–77]; however, there is no information found concerning the two-photon photoluminescence of a-C film, unlike the one-photon excitation.

Two-photon-excited luminescence of NDs can also be influenced by plasmonic metal. For example, the plasmon-enhanced luminescence of SiV-doped NDs at the two-photon absorption at a 830 nm wavelength laser excitation was observed [67]. The FLIM of a-C:ND/Ag (Figure 9b-II) looks qualitatively similar to the FLIM of a-C:ND, and the character of both images indicates the embedding of luminescent particles or their clusters in a nonluminescent matrix. The luminescence of both a-C:ND and a-C:ND/Ag has a very short lifetime of about 0.1 ns, which is quite typical for the previously observed ND luminescence excited by two-photon absorption and emitted in the range of 450–640 nm [78]. However, as Figure 9a,c shows, the signal intensity was significantly higher in the case of a-C:ND/Ag.

Thus, we can conclude that two-photon luminescence is mostly observed from the ND particles in the a-C:ND films. This result is in agreement with the obtained spectra of plasmon-enhanced one-photon luminescence, which allows us to conclude that two-photon luminescence originates from NV centers (particularly, the NV<sup>0</sup> with the zero-phonon line (ZPL) at 575 nm and the sideband centered at 600 nm) in NDs. However, the PL from other defects, e.g., H3 (with the ZPL at 503 nm), H4 (with the ZPL at 496 nm), the sideband of NV<sup>-</sup> PL as well as a nonstructured PL from the ND surface, also falls within the detected spectral interval of 450–640 nm.

Figure 9c shows the histograms of the lifetime distribution of individual particles or clusters visible in the FLIM images of the a-C:ND and the a-C:ND/Ag from the observed area. The TPL intensity was revealed via count numbers for the luminescent nanocarbon particles with and without interaction with Ag.

The intensity of the a-C:ND/Ag TPL compared with the TPL of a-C:ND increased about two to five times for some particles; however, for some points, it might be dozens of times higher. Note that although some plasmonic metals can demonstrate an intense TPL [79], we did not observe it from the prepared AgNP, so it did not overlap with the enhanced TPL of the NDs embedded in the a-C:ND.

### 3.5. Assessment of the DND Antibacterial and Antifungal Effect

The use of the antibacterial properties of nanostructures is currently considered an alternative to the antibiotics loaded in the antibacterial coatings of implants and medical materials in order to prevent infection and accelerate wound healing in antibiotic delivery systems for the treatment of diseases, diagnostic systems, etc. As for NDs, their application as a highly promising antibiotics alternative was analyzed in [80].

As the first step in the estimation of the biomedical potential of synthesized film with uniformly distributed DNDs, the antimicrobial activity of the DNDs was assessed (Table 2). The test sample showed weak antimicrobial activity against gram-positive bacteria *B. subtilis* ATCC 6633, *S. aureus* 209P, and gram-negative bacteria *E. coli* ATCC 25922. There was no activity detected by this method for *M. luteus* NCTC 8340 and gram-negative bacteria *P. aeruginosa* ATCC 27853. Interestingly, activity was detected for all the test strains of fungi: *A. niger* INA 00760, *A. fumigatus* KPB F-37, and yeast *C. albicans* ATCC 2091. Note that although only a weak activity was detected, this result can be determined by the low ability of DNDs to diffuse on agar compared with a higher diffusivity of the control antibiotics. The antibacterial mechanisms of nanoparticles are still poorly understood [80]. There are only some preliminary suggestions. Thus, previously for gram-negative *E. coli*, it was shown that small-size ND particles can cause the mechanical destruction of a cell wall resulting in cell death [81].

While recently, the bactericidal properties of nanostructures (firstly, nanoparticles), including nanocarbons [82–84], have been investigated, only one paper concerning the effect of nanodiamonds on *C. albicans*'s adhesion on materials applied in dentistry was published [85]. There is no comprehensive study related to the interaction between nanos-

structures and fungi, although the risk factors of fungal infection (prolonged stays in an intensive care unit, mechanical ventilation, broad-spectrum antibiotic therapy, central venous line insertion, etc.) are frequent in severe burn care, predisposing to potentially serious fungal wound infections related or unrelated to bacterial infection [86,87]. Thus, alternative materials with antifungal activity are no less important than antibacterial ones.

**Table 2.** Antimicrobial activity of DNDs.

	<i>B. subtilis</i> ATCC 6633	<i>P. aeruginosa</i> ATCC 27853	<i>M. luteus</i> NCTC 8340	<i>S. aureus</i> 209	<i>E. coli</i> ATCC 25922	<i>A. niger</i> INA 00760	<i>C. albicans</i> ATCC 2091	<i>A. fumigatus</i> KPB F-37
DND	11 ± 0.2	0	0	9 ± 0.1	11 ± 0.1	11 ± 0.3	11 ± 0.2	11 ± 0.1
amoxiclav	18 ± 0.4	11 ± 0.2	24 ± 0.1	25 ± 0.3	11 ± 0.1	nt *	nt *	nt *
amphotericin B	nt *	nt *	nt *	nt *	nt *	17 ± 0.1	11 ± 0.09	10 ± 0.1

\* nt—nontested.

Although nanoparticles are currently considered to be promising antibiotics alternatives, some aspects of their antibacterial mechanisms are yet to be investigated, so further development of the analytical potential of synthesized a-C:ND and a-C:ND/Ag can contribute to this research.

Nanocarbons and nanocarbon-based hybrids showed significant antibacterial activity depending on their physical and chemical properties, size, and surface structure [81–84,88–96]. The possibility of modifying the properties of the film and embedded NP allows the optimization of the antimicrobial effect. Particularly, a good dispersion of NDs in the matrix may be important, as it was shown previously that the antibacterial efficiency of nanoparticles decreases at their aggregation [92,97].

The detrimental effects of NDs on microorganisms were previously observed in a more significant volume for the NDs with a higher content of sp<sup>2</sup>-carbon on the surface [96,98]; thus, we can suggest that distribution in the a-C film will not decrease antimicrobial properties of DNDs notably [99]. However, further study and optimization of the a-C:ND film is needed to assess its biomedical potential and applicability.

#### 4. Key Findings

- (1) Microarc-assisted magnetron sputtering of the DND powder in pulsed mode was applied to manufacture the coating of NDs encapsulated in an amorphous carbon matrix, i.e., a-C:ND structure. EELS showed that the cumulative sp<sup>3</sup>/(sp<sup>2</sup> + sp<sup>3</sup>) ratio of a-C:ND was 76%.
- (2) SEM and TEM revealed spatial uniformity of the distribution of encapsulated NDs and an absence of the NDs' aggregation, thus resulting in good dispersion of the NDs in the a-C:ND structures.
- (3) The plasmonic properties of AgNP formed by low-energy Ar<sup>+</sup> irradiation of continuous Ag film allowed us to observe the SERS effect on an a-C:ND/Ag structure. Spectra intensity enhancement only occurred several times, and a selective SERS sensitivity to nondiamond sp<sup>2</sup>-features was observed.
- (4) SERS studies indicated that ion irradiation of the Ag overlayer had only slightly changed the D and G lines of an a-C:ND film, proving that the suggested technique of the plasmonic-active structure formation had not altered the analyzed structure.
- (5) Two-photon-excited luminescence was observed from the ND particles both in a-C:ND and a-C:ND/Ag at near-infrared excitation with fs laser. The luminescence lifetime in both cases was ~< 0.1 ns. While the lifetime did not change as a result of the plasmon-enhanced study, increased Ag-modified TPL intensity was observed for a-C:ND/Ag in comparison with a-C:ND.
- (6) The agar diffusion method revealed the prominent inhibition effect of DNDs against the bacterial strains of *B. subtilis*, *S. aureus*, *E. coli* as well as against all of the test fungi strains (*A. niger*, *C. albicans*, and *A. fumigatu*).

## 5. Conclusions and Outlook

In conclusion, the synthesis of nanocarbon structures with preset configuration was demonstrated. The resulting a-C:ND film consisted of amorphous carbon film with embedded, well-dispersed nanodiamond particles. The structure and spectral properties of a-C:ND were analyzed.

The plasmonic-active Ag nanoparticle layer was formed on the a-C:ND film via the irradiation of magnetron-deposited Ag film by low-energy Ar<sup>+</sup> ions. It was demonstrated that the suggested ion-beam modification technique is a promising way to create a SERS-active media for the plasmon-enhanced analysis of organic structures.

The plasmonic properties of Ag allowed us to get additional information about a-C:ND structure due to the observed SERS of carbon with sp<sup>2</sup> hybridization. Thus, the SERS characterization gives information on nondiamond features in the vicinity of NDs and on their surface.

Ag-modified luminescence of the embedded ND was observed at an excitation of 532 nm wavelength, characteristic for NV<sup>0</sup> color centers with the possible contribution of other structural defects, such as surface defects whose emission was in the corresponding spectral range. Two-photon-excited luminescence was observed from embedded ND particles or their clusters both in a-C:ND and a-C:ND/Ag at near-infrared excitation with fs laser. The lifetime of the luminescence in both cases was about or less than 0.1 ns. While the lifetime did not change as a result of the plasmon-enhanced study, an increasing TPL intensity was observed for a-C:ND/Ag in comparison with a-C:ND.

The presented method of nanocarbon structure synthesis and the characterization of prepared structures allows further development of the technique for obtaining carbon-silver nanohybrid of modified preset properties. The reported nanotechnology allows further research and development in the field of bactericidal properties of nanodiamonds [82]. Plasmon-enhanced Raman (SERS) and luminescence spectroscopy of ND–Ag nanohybrids have the potential to reveal new data concerning the mechanism of bacterial membrane rupture during the interactions with nanodiamonds.

The antimicrobial properties of DNDs as a part of the hybrid structure were tested. A prominent inhibition effect was observed for a number of bacteria and all the test strains of fungi. This makes the structure with embedded DNDs a prospect for the development of antibacterial coatings. The a-C:ND hybrid may be promising for spectroscopic studies on the interaction between both pathogenic and nonpathogenic microorganisms and the carbon nanostructure.

**Author Contributions:** Conceptualization, O.S., E.P. and V.S. (Vera Sadykova); methodology, O.S., E.P., A.K. (Artashes Karmenyan) and V.S. (Vera Sadykova); software, I.Z., A.K. (Artashes Karmenyan) and A.K. (Anastasia Kuvarina); validation, V.S. (Vladimir Sychev), V.S. (Vera Sadykova), E.P. and C.-L.C.; formal analysis, E.P., A.K. (Anastasia Kuvarina), I.Z., V.S. (Vladimir Sychev) and O.S.; investigation, O.S., E.P., A.K. (Artashes Karmenyan), V.S. (Vladimir Sychev) and A.K. (Anastasia Kuvarina); resources, O.S., E.P., V.S. (Vera Sadykova) and C.-L.C.; data curation, E.P., I.Z. and V.S. (Vladimir Sychev); writing—original draft preparation, E.P., I.Z. and V.S. (Vera Sadykova); writing—review and editing, I.Z., V.S. (Vladimir Sychev) and A.K. (Artashes Karmenyan); visualization, I.Z., A.K. (Artashes Karmenyan); supervision, O.S., E.P. and C.-L.C.; project administration, E.P., C.-L.C., V.S. (Vera Sadykova) and O.S.; funding acquisition, C.-L.C., I.Z. All authors have read and agreed to the published version of the manuscript.

**Funding:** This research has been supported by the Interdisciplinary Scientific and Educational School of Moscow University «Photonic and Quantum technologies. Digital medicine» and by the grant of MOST, Taiwan, number 109-2112-M-259-005-MY3. Ilya Zavidovskiy acknowledges the support of the Basis Foundation fellowship program, grant 20-2-2-7-1.

**Institutional Review Board Statement:** Not applicable.

**Informed Consent Statement:** Not applicable.

**Data Availability Statement:** The data presented in this study are available on request from the corresponding author.

**Conflicts of Interest:** The authors declare no conflict of interest. The funders had no role in the design of the study; in the collection, analyses, or interpretation of data; in the writing of the manuscript; or in the decision to publish the results.

## References

1. Li, C.-C.; Huang, C.-L. Preparation of Clear Colloidal Solutions of Detonation Nanodiamond in Organic Solvents. *Colloids Surf. A Physicochem. Eng. Asp.* **2010**, *353*, 52–56. [[CrossRef](#)]
2. Kulakova, I.I. Surface Chemistry of Nanodiamonds. *Phys. Solid State* **2004**, *46*, 636–643. [[CrossRef](#)]
3. Vejpravová, J. Mixed Sp<sup>2</sup>–Sp<sup>3</sup> Nanocarbon Materials: A Status Quo Review. *Nanomaterials* **2021**, *11*, 2469. [[CrossRef](#)]
4. Shvidchenko, A.V.; Eidelman, E.D.; Vul', A.Y.; Kuznetsov, N.M.; Stolyarova, D.Y.; Belousov, S.I.; Chvalun, S.N. Colloids of Detonation Nanodiamond Particles for Advanced Applications. *Adv. Colloid Interface Sci.* **2019**, *268*, 64–81. [[CrossRef](#)]
5. Sivtsov, E.V.; Kalinin, A.V.; Gostev, A.I.; Smirnov, A.V.; Agibalova, L.V.; Shumilov, F.A. In Situ Preparation of Polymer Nanocomposites Based on Sols of Surface-Modified Detonation Nanodiamonds by Classical and Controlled Radical Polymerization. *Polym. Sci. Ser. B* **2020**, *62*, 734–749. [[CrossRef](#)]
6. Streletskiy, O.A.; Zavidovskiy, I.A.; Sychev, V.V.; Dudin, A.A.; Savinov, S.A.; Pavlikov, A.V. Magnetron Deposition of A-C:ND Coatings by Nanodiamond Transfer: Pulse Number Impact on Aggregation and Graphitization. *Appl. Phys. A* **2022**, *128*, 83. [[CrossRef](#)]
7. Lenzini, F.; Gruhler, N.; Walter, N.; Pernice, W.H.P. Diamond as a Platform for Integrated Quantum Photonics. *Adv. Quantum Technol.* **2018**, *1*, 1800061. [[CrossRef](#)]
8. Chen, Y.G.; Ogura, M.; Okushi, H. Schottky Junction Properties on High Quality Boron-Doped Homoepitaxial Diamond Thin Films. *J. Vac. Sci. Technol. B Microelectron. Nanometer Struct. Processing Meas. Phenom.* **2004**, *22*, 2084–2086. [[CrossRef](#)]
9. Basso, L.; Cazzanelli, M.; Orlandi, M.; Miotello, A. Nanodiamonds: Synthesis and Application in Sensing, Catalysis, and the Possible Connection with Some Processes Occurring in Space. *Appl. Sci.* **2020**, *10*, 4094. [[CrossRef](#)]
10. Petráková, V.; Taylor, A.; Kratochvílová, I.; Fendrych, F.; Vacík, J.; Kučka, J.; Štursa, J.; Cígler, P.; Ledvina, M.; Fišerová, A.; et al. Luminescence of Nanodiamond Driven by Atomic Functionalization: Towards Novel Detection Principles. *Adv. Funct. Mater.* **2012**, *22*, 812–819. [[CrossRef](#)]
11. Hui, Y.Y.; Chen, O.Y.; Azuma, T.; Chang, B.-M.; Hsieh, F.-J.; Chang, H.-C. All-Optical Thermometry with Nitrogen-Vacancy Centers in Nanodiamond-Embedded Polymer Films. *J. Phys. Chem. C* **2019**, *123*, 15366–15374. [[CrossRef](#)]
12. Tallaire, A.; Brinza, O.; De Feudis, M.; Ferrier, A.; Touati, N.; Binet, L.; Nicolas, L.; Delord, T.; Hétet, G.; Herzig, T.; et al. Synthesis of Loose Nanodiamonds Containing Nitrogen-Vacancy Centers for Magnetic and Thermal Sensing. *ACS Appl. Nano Mater.* **2019**, *2*, 5952–5962. [[CrossRef](#)]
13. Iyer, A.; Etula, J.; Ge, Y.; Liu, X.; Koskinen, J. Nanodiamond Embedded Ta-C Composite Film by Pulsed Filtered Vacuum Arc Deposition from a Single Target. *Appl. Phys. Lett.* **2016**, *109*, 201905. [[CrossRef](#)]
14. Claveau, S.; Bertrand, J.-R.; Treussart, F. Fluorescent Nanodiamond Applications for Cellular Process Sensing and Cell Tracking. *Micromachines* **2018**, *9*, 247. [[CrossRef](#)] [[PubMed](#)]
15. Lin, Y.-C.; Tsai, L.-W.; Perevedentseva, E.; Karmenyan, A.; Cheng, C.-L. Near-Infrared Fluorescence from Nanodiamond for Multimodal Bioimaging. *Sovrem. Tehnol. V Med.* **2018**, *10*, 49–56. [[CrossRef](#)]
16. Tisler, J.; Reuter, R.; Lämmle, A.; Jelezko, F.; Balasubramanian, G.; Hemmer, P.R.; Reinhard, F.; Wrachtrup, J. Highly Efficient FRET from a Single Nitrogen-Vacancy Center in Nanodiamonds to a Single Organic Molecule. *ACS Nano* **2011**, *5*, 7893–7898. [[CrossRef](#)]
17. Börsch, M.; Reuter, R.; Balasubramanian, G.; Erdmann, R.; Jelezko, F.; Wrachtrup, J. Fluorescent Nanodiamonds for FRET-Based Monitoring of a Single Biological Nanomotor FoF1-ATP Synthase. In Proceedings of the Multiphoton Microscopy in the Biomedical Sciences IX, SPIE, San Jose, CA, USA, 13 February 2009; Volume 7183, pp. 496–505.
18. Wang, Y.; Wang, L.; Wang, S.C.; Zhang, G.; Wood, R.J.K.; Xue, Q. Nanocomposite Microstructure and Environment Self-Adapted Tribological Properties of Highly Hard Graphite-Like Film. *Tribol. Lett.* **2010**, *40*, 301–310. [[CrossRef](#)]
19. Naragino, H.; Egiza, M.; Tominaga, A.; Murasawa, K.; Gonda, H.; Sakurai, M.; Yoshitake, T. Hard Coating of Ultrananocrystalline Diamond/Nonhydrogenated Amorphous Carbon Composite Films on Cemented Tungsten Carbide by Coaxial Arc Plasma Deposition. *Appl. Phys. A* **2016**, *122*, 761. [[CrossRef](#)]
20. Ali, A.M.; Deckert-Gaudig, T.; Egiza, M.; Deckert, V.; Yoshitake, T. Near- and Far-Field Raman Spectroscopic Studies of Nanodiamond Composite Films Deposited by Coaxial Arc Plasma. *Appl. Phys. Lett.* **2020**, *116*, 041601. [[CrossRef](#)]
21. Ali, A.M.; Egiza, M.; Murasawa, K.; Sugita, H.; Deckert-Gaudig, T.; Deckert, V.; Yoshitake, T. Effects of Substrate Temperature and Intermediate Layer on Adhesion, Structural and Mechanical Properties of Coaxial Arc Plasma Deposition Grown Nanodiamond Composite Films on Si Substrates. *Surf. Coat. Technol.* **2021**, *417*, 127185. [[CrossRef](#)]
22. Takeichi, S.; Nishiyama, T.; Tabara, M.; Kawawaki, S.; Kohno, M.; Takahashi, K.; Yoshitake, T. Thermal Conductivity of Ultrananocrystalline Diamond/Hydrogenated Amorphous Carbon Composite Films Prepared by Coaxial Arc Plasma Deposition. *ECS Trans.* **2017**, *75*, 27. [[CrossRef](#)]
23. Shaban, M. Determination of Trap Density-of-States Distribution of Nitrogen-Doped Ultrananocrystalline Diamond/Hydrogenated Amorphous Carbon Composite Films. *J. Semicond.* **2021**, *42*, 062802–062807. [[CrossRef](#)]
24. Nistor, P.A.; May, P.W. Diamond Thin Films: Giving Biomedical Applications a New Shine. *J. R. Soc. Interface* **2017**, *14*, 20170382. [[CrossRef](#)] [[PubMed](#)]

25. Islam, M.; Lantada, A.D.; Mager, D.; Korvink, J.G. Carbon-Based Materials for Articular Tissue Engineering: From Innovative Scaffolding Materials toward Engineered Living Carbon. *Adv. Healthc. Mater.* **2022**, *11*, 2101834. [[CrossRef](#)] [[PubMed](#)]
26. Carvalho, I.; Rodrigues, L.; Lima, M.J.; Carvalho, S.; Cruz, S.M.A. Overview on the Antimicrobial Activity and Biocompatibility of Sputtered Carbon-Based Coatings. *Processes* **2021**, *9*, 1428. [[CrossRef](#)]
27. Kaneko, M.; Hiratsuka, M.; Alanazi, A.; Nakamori, H.; Namiki, K.; Hirakuri, K. Surface Reformation of Medical Devices with DLC Coating. *Materials* **2021**, *14*, 376. [[CrossRef](#)]
28. Novikov, S.M.; Streletskiy, O.A.; Doroshina, N.V.; Yakubovsky, D.I.; Mironov, M.S.; Sychev, V.V.; Voronov, A.A.; Arsenin, A.V.; Volkov, V.S. Long-Term Stable Structures Formed by Ion-Beam Modification of Silver Film for SERS Applications. *J. Phys. Conf. Ser.* **2021**, *2015*, 012099. [[CrossRef](#)]
29. Streletskiy, O.; Zavidovskiy, I.; Yakubovsky, D.; Doroshina, N.; Syuy, A.; Lebedinskij, Y.; Markeev, A.; Arsenin, A.; Volkov, V.; Novikov, S. Tailoring of the Distribution of SERS-Active Silver Nanoparticles by Post-Deposition Low-Energy Ion Beam Irradiation. *Materials* **2022**, *15*, 7721. [[CrossRef](#)]
30. Veres, M.; Füle, M.; Tóth, S.; Koós, M.; Pócsik, I. Surface Enhanced Raman Scattering (SERS) Investigation of Amorphous Carbon. *Diam. Relat. Mater.* **2004**, *13*, 1412–1415. [[CrossRef](#)]
31. Nascimento, G.M.D. *Raman Spectroscopy*; IntechOpen: London, UK, 2018; ISBN 978-1-78923-000-0. [[CrossRef](#)]
32. Karmenyan, A.V.; Perevedentseva, E.; Veres, M.; Cheng, C.-L. Simultaneous Photoluminescence and SERS Observation of Nanodiamond at Laser Deposition on Noble Metals. *Plasmonics* **2013**, *8*, 325–333. [[CrossRef](#)]
33. European Committee on Antimicrobial Susceptibility Testing Antimicrobial Susceptibility Testing. EUCAST Disk Diffusion Method. Available online: [https://www.eucast.org/fileadmin/src/media/PDFs/EUCAST\\_files/Disk\\_test\\_documents/2021\\_manuals/Manual\\_v\\_9.0\\_EUCAST\\_Disk\\_Test\\_2021.pdf](https://www.eucast.org/fileadmin/src/media/PDFs/EUCAST_files/Disk_test_documents/2021_manuals/Manual_v_9.0_EUCAST_Disk_Test_2021.pdf) (accessed on 31 October 2022).
34. Yang, B.; Li, J.; Guo, L.; Huang, N.; Liu, L.; Zhai, Z.; Long, W.; Jiang, X. Fabrication of Silicon-Vacancy Color Centers in Diamond Films: Tetramethylsilane as a New Dopant Source. *CrystEngComm* **2018**, *20*, 1158–1167. [[CrossRef](#)]
35. Noborisaka, M.; Horikoshi, R.; Nagashima, S.; Shirakura, A.; Suzuki, T. Hardness and Surface Roughness of Hydrogenated Amorphous Carbon-Based Films Synthesized by Atmospheric Pressure-Plasma Enhanced Chemical Vapor Deposition at Low Temperature. *Thin Solid Film.* **2013**, *527*, 114–119. [[CrossRef](#)]
36. Simonot, L.; Chabanais, F.; Rousselet, S.; Pailloux, F.; Camelio, S.; Babonneau, D. Evolution of Plasmonic Nanostructures under Ultra-Low-Energy Ion Bombardment. *Appl. Surf. Sci.* **2021**, *544*, 148672. [[CrossRef](#)]
37. Klimmer, A.; Ziemann, P.; Biskupek, J.; Kaiser, U.; Fleisch, M. Size-Dependent Effect of Ion Bombardment on Au Nanoparticles on Top of Various Substrates: Thermodynamically Dominated Capillary Forces versus Sputtering. *Phys. Rev. B* **2009**, *79*, 155427. [[CrossRef](#)]
38. Murty, M.V.R. Sputtering: The Material Erosion Tool. *Surf. Sci.* **2002**, *500*, 523–544. [[CrossRef](#)]
39. Resta, V.; Peláez, R.J.; Afonso, C.N. Importance of Ion Bombardment during Coverage of Au Nanoparticles on Their Structural Features and Optical Response. *J. Appl. Phys.* **2014**, *115*, 124303. [[CrossRef](#)]
40. Nest, D.; Graves, D.B.; Engelmann, S.; Bruce, R.L.; Weilnboeck, F.; Oehrlein, G.S.; Andes, C.; Hudson, E.A. Synergistic Effects of Vacuum Ultraviolet Radiation, Ion Bombardment, and Heating in 193nm Photoresist Roughening and Degradation. *Appl. Phys. Lett.* **2008**, *92*, 153113. [[CrossRef](#)]
41. Soltys, L.; Olkhovyy, O.; Tatarchuk, T.; Naushad, M. Green Synthesis of Metal and Metal Oxide Nanoparticles: Principles of Green Chemistry and Raw Materials. *Magnetochemistry* **2021**, *7*, 145. [[CrossRef](#)]
42. Dobrev, D. Ion-Beam-Induced Texture Formation in Vacuum-Condensed Thin Metal Films. *Thin Solid Film.* **1982**, *92*, 41–53. [[CrossRef](#)]
43. Novikov, S.M.; Popok, V.N.; Evlyukhin, A.B.; Hanif, M.; Morgen, P.; Fiutowski, J.; Beermann, J.; Rubahn, H.-G.; Bozhevolnyi, S.I. Highly Stable Monocrystalline Silver Clusters for Plasmonic Applications. *Langmuir* **2017**, *33*, 6062–6070. [[CrossRef](#)]
44. Starowicz, Z.; Wojnarowska-Nowak, R.; Ozga, P.; Sheregii, E.M. The Tuning of the Plasmon Resonance of the Metal Nanoparticles in Terms of the SERS Effect. *Colloid. Polym. Sci.* **2018**, *296*, 1029–1037. [[CrossRef](#)] [[PubMed](#)]
45. Jensen, T.; Kelly, L.; Lazarides, A.; Schatz, G.C. Electrodynamics of Noble Metal Nanoparticles and Nanoparticle Clusters. *J. Clust. Sci.* **1999**, *10*, 295–317. [[CrossRef](#)]
46. Shanthil, M.; Thomas, R.; Swathi, R.S.; George Thomas, K. Ag@SiO<sub>2</sub> Core-Shell Nanostructures: Distance-Dependent Plasmon Coupling and SERS Investigation. *J. Phys. Chem. Lett.* **2012**, *3*, 1459–1464. [[CrossRef](#)]
47. Cortijo-Campos, S.; Ramírez-Jiménez, R.; Climent-Pascual, E.; Aguilar-Pujol, M.; Jiménez-Villacorta, F.; Martínez, L.; Jiménez-Riobóo, R.; Prieto, C.; de Andrés, A. Raman Amplification in the Ultra-Small Limit of Ag Nanoparticles on SiO<sub>2</sub> and Graphene: Size and Inter-Particle Distance Effects. *Mater. Des.* **2020**, *192*, 108702. [[CrossRef](#)] [[PubMed](#)]
48. Praver, S.; Nemanich, R.J. Raman Spectroscopy of Diamond and Doped Diamond. *Philos. Trans. R. Soc. London. Ser. A Math. Phys. Eng. Sci.* **2004**, *362*, 2537–2565. [[CrossRef](#)]
49. Dychalska, A.; Popielarski, P.; Franków, W.; Fabisiak, K.; Paprocki, K.; Szybowski, M. Study of CVD Diamond Layers with Amorphous Carbon Admixture by Raman Scattering Spectroscopy. *Mater. Sci.* **2015**, *33*, 799–805. [[CrossRef](#)]
50. Knight, D.S.; Weimer, R.; Pilione, L.; White, W.B. Surface-enhanced Raman Spectroscopy of Chemical Vapor Deposited Diamond Films. *Appl. Phys. Lett.* **1990**, *56*, 1320–1322. [[CrossRef](#)]
51. Demirel, G.; Usta, H.; Yilmaz, M.; Celik, M.; Alidagi, H.A.; Buyukserin, F. Surface-Enhanced Raman Spectroscopy (SERS): An Adventure from Plasmonic Metals to Organic Semiconductors as SERS Platforms. *J. Mater. Chem. C* **2018**, *6*, 5314–5335. [[CrossRef](#)]

52. Ferrari, A.C.; Robertson, J. Interpretation of Raman Spectra of Disordered and Amorphous Carbon. *Phys. Rev. B* **2000**, *61*, 14095–14107. [[CrossRef](#)]
53. Ferrari, A.C.; Robertson, J. Origin of the 1150  $\text{cm}^{-1}$  Raman Mode in Nanocrystalline Diamond. *Phys. Rev. B* **2001**, *63*, 121405. [[CrossRef](#)]
54. Zhang, D.; Zhang, R.Q. Signature of Nanodiamond in Raman Spectra: A Density Functional Theoretical Study. *J. Phys. Chem. B* **2005**, *109*, 9006–9013. [[CrossRef](#)] [[PubMed](#)]
55. Zavidovskiy, I.A.; Streletskiy, O.A.; Nishchak, O.Y.; Haidarov, A.A.; Pavlikov, A.V. The Influence of Ion Assistance Energy on Structural and Optical Properties of Carbon-Silver Nanocomposites. *Thin Solid Film.* **2021**, *738*, 138966. [[CrossRef](#)]
56. Kasuya, A.; Sasaki, Y.; Saito, Y.; Tohji, K.; Nishina, Y. Evidence for Size-Dependent Discrete Dispersions in Single-Wall Nanotubes. *Phys. Rev. Lett.* **1997**, *78*, 4434–4437. [[CrossRef](#)]
57. Mews, A.; Koberling, F.; Basché, T.; Philipp, G.; Duesberg, G.; Roth, S.; Burghard, M. Raman Imaging of Single Carbon Nanotubes. *Adv. Mater.* **2000**, *12*, 1210–1214. [[CrossRef](#)]
58. Claramunt, S.; Varea, A.; López-Díaz, D.; Velázquez, M.M.; Cornet, A.; Cirera, A. The Importance of Interbands on the Interpretation of the Raman Spectrum of Graphene Oxide. *J. Phys. Chem. C* **2015**, *119*, 10123–10129. [[CrossRef](#)]
59. Caro, M.A.; Deringer, V.L.; Koskinen, J.; Laurila, T.; Csányi, G. Growth Mechanism and Origin of High  $\text{Sp}^3$  Content in Tetrahedral Amorphous Carbon. *Phys. Rev. Lett.* **2018**, *120*, 166101. [[CrossRef](#)]
60. Wang, S.; Komvopoulos, K. A Molecular Dynamics Study of the Oxidation Mechanism, Nanostructure Evolution, and Friction Characteristics of Ultrathin Amorphous Carbon Films in Vacuum and Oxygen Atmosphere. *Sci. Rep.* **2021**, *11*, 3914. [[CrossRef](#)]
61. Streletskiy, O.A.; Zavidovskiy, I.A.; Balabanyan, V.Y.; Tsiskarashvili, A.V. Antibacterial Properties of Modified A-C and Ta-C Coatings: The Effects of the  $\text{Sp}^2/\text{Sp}^3$  Ratio, Oxidation, Nitridation, and Silver Incorporation. *Appl. Phys. A* **2022**, *128*, 929. [[CrossRef](#)]
62. Vlasov, I.I.; Shenderova, O.A. Raman and Photoluminescence Spectroscopy of Detonation Nanodiamonds. In *Detonation Nanodiamonds*; Jenny Stanford Publishing: Stanford, CA, USA, 2013; ISBN 978-0-429-16896-3. [[CrossRef](#)]
63. Aleksenskii, A.E.; Osipov, V.Y.; Vul', A.Y.; Ber, B.Y.; Smirnov, A.B.; Melekhin, V.G.; Adriaenssens, G.J.; Iakubovskii, K. Optical Properties of Nanodiamond Layers. *Phys. Solid State* **2001**, *43*, 145–150. [[CrossRef](#)]
64. Hu, S.; Guo, Y.; Dong, Y.; Yang, J.; Liu, J.; Cao, S. Understanding the Effects of the Structures on the Energy Gaps in Carbon Nanoparticles from Laser Synthesis. *J. Mater. Chem.* **2012**, *22*, 12053–12057. [[CrossRef](#)]
65. Reineck, P.; Lau, D.W.M.; Wilson, E.R.; Fox, K.; Field, M.R.; Deeleeppojananan, C.; Mochalin, V.N.; Gibson, B.C. Effect of Surface Chemistry on the Fluorescence of Detonation Nanodiamonds. *ACS Nano* **2017**, *11*, 10924–10934. [[CrossRef](#)] [[PubMed](#)]
66. Lim, T.-S.; Fu, C.-C.; Lee, K.-C.; Lee, H.-Y.; Chen, K.; Cheng, W.-F.; Wu, W.P.; Chang, H.-C.; Fann, W. Fluorescence Enhancement and Lifetime Modification of Single Nanodiamonds near a Nanocrystalline Silver Surface. *Phys. Chem. Chem. Phys.* **2009**, *11*, 1508–1514. [[CrossRef](#)] [[PubMed](#)]
67. Song, J.; Li, H.; Lin, F.; Wang, L.; Wu, H.; Yang, Y. Plasmon-Enhanced Photoluminescence of Si-V Centers in Diamond from a Nanoassembled Metal–Diamond Hybrid Structure. *CrystEngComm* **2014**, *16*, 8356–8362. [[CrossRef](#)]
68. Andersen, S.K.H.; Kumar, S.; Bozhevolnyi, S.I. Coupling of Nitrogen-Vacancy Centers in a Nanodiamond to a Silver Nanocube. *Opt. Mater. Express OME* **2016**, *6*, 3394–3406. [[CrossRef](#)]
69. Gong, J.; Steinsultz, N.; Ouyang, M. Nanodiamond-Based Nanostructures for Coupling Nitrogen-Vacancy Centres to Metal Nanoparticles and Semiconductor Quantum Dots. *Nat. Commun.* **2016**, *7*, 11820. [[CrossRef](#)]
70. Li, J.; Zhang, B.; Wang, F.; Liu, C. Silver/Carbon-Quantum-Dot Plasmonic Luminescent Nanoparticles. *New J. Chem.* **2011**, *35*, 554–557. [[CrossRef](#)]
71. Bagra, B.; Zhang, W.; Zeng, Z.; Mabe, T.; Wei, J. Plasmon-Enhanced Fluorescence of Carbon Nanodots in Gold Nanoslit Cavities. *Langmuir* **2019**, *35*, 8903–8909. [[CrossRef](#)]
72. Tóth, S.; Fule, M.; Veres, M.; Koós, M. Photoluminescence in Carbon-Based Amorphous Materials. In *Optics and Electro-Optics Research*; Nova Science Publishers, Inc.: New York, NY, USA, 2007; pp. 225–247. ISBN 978-1-60021-682-4.
73. Fedotov, I.V.; Zheltikov, A.M. Background-Free Two-Photon Fluorescence Readout via a Three-Photon Charge-State Modulation of Nitrogen-Vacancy Centers in Diamond. *Opt. Lett.* **2019**, *44*, 3737–3740. [[CrossRef](#)]
74. Johnstone, G.E.; Cairns, G.S.; Patton, B.R. Nanodiamonds Enable Adaptive-Optics Enhanced, Super-Resolution, Two-Photon Excitation Microscopy. *R. Soc. Open Sci.* **2019**, *6*, 190589. [[CrossRef](#)]
75. Pan, L.; Sun, S.; Zhang, L.; Jiang, K.; Lin, H. Near-Infrared Emissive Carbon Dots for Two-Photon Fluorescence Bioimaging. *Nanoscale* **2016**, *8*, 17350–17356. [[CrossRef](#)]
76. Lan, M.; Zhao, S.; Zhang, Z.; Yan, L.; Guo, L.; Niu, G.; Zhang, J.; Zhao, J.; Zhang, H.; Wang, P.; et al. Two-Photon-Excited near-Infrared Emissive Carbon Dots as Multifunctional Agents for Fluorescence Imaging and Photothermal Therapy. *Nano Res.* **2017**, *10*, 3113–3123. [[CrossRef](#)]
77. Pramanik, A.; Fan, Z.; Chavva, S.R.; Sinha, S.S.; Ray, P.C. Highly Efficient and Excitation Tunable Two-Photon Luminescence Platform For Targeted Multi-Color MDRB Imaging Using Graphene Oxide. *Sci. Rep.* **2014**, *4*, 6090. [[CrossRef](#)] [[PubMed](#)]
78. Perevedentseva, E.; Ali, N.; Karmenyan, A.; Skovorodkin, I.; Prunskaitė-Hyyryläinen, R.; Vainio, S.; Cheng, C.-L.; Kinnunen, M. Optical Studies of Nanodiamond-Tissue Interaction: Skin Penetration and Localization. *Materials* **2019**, *12*, 3762. [[CrossRef](#)] [[PubMed](#)]

79. Melentiev, P.N.; Afanasiev, A.E.; Kuzin, A.A.; Zablotskiy, A.V.; Balykin, V.I. Giant Enhancement of Two Photon Induced Luminescence in Metal Nanostructure. *Opt. Express OE* **2015**, *23*, 11444–11452. [[CrossRef](#)]
80. Cumont, A.; Pitt, A.R.; Lambert, P.A.; Oggioni, M.R.; Ye, H. Properties, Mechanism and Applications of Diamond as an Antibacterial Material. *Funct. Diam.* **2021**, *1*, 1–28. [[CrossRef](#)]
81. Chatterjee, A.; Perevedentseva, E.; Jani, M.; Cheng, C.-Y.; Ye, Y.-S.; Chung, P.-H.; Cheng, C.-L. Antibacterial Effect of Ultrafine Nanodiamond against Gram-Negative Bacteria *Escherichia coli*. *J. Biomed. Opt.* **2014**, *20*, 051014. [[CrossRef](#)]
82. Szunerits, S.; Barras, A.; Boukherroub, R. Antibacterial Applications of Nanodiamonds. *Int. J. Environ. Res. Public Health* **2016**, *13*, 413. [[CrossRef](#)]
83. Wang, C.; Makvandi, P.; Zare, E.N.; Tay, F.R.; Niu, L. Advances in Antimicrobial Organic and Inorganic Nanocompounds in Biomedicine. *Adv. Ther.* **2020**, *3*, 2000024. [[CrossRef](#)]
84. Torres Sangiao, E.; Holban, A.M.; Gestal, M.C. Applications of Nanodiamonds in the Detection and Therapy of Infectious Diseases. *Materials* **2019**, *12*, 1639. [[CrossRef](#)]
85. Fouda, S.M.; Gad, M.M.; Ellakany, P.; Al-Thobity, A.M.; Al-Harbi, F.A.; Virtanen, J.I.; Raustia, A. The Effect of Nanodiamonds on *Candida albicans* Adhesion and Surface Characteristics of PMMA Denture Base Material—An in Vitro Study. *J. Appl. Oral Sci.* **2019**, *27*, e20180779. [[CrossRef](#)]
86. Pruskowski, K.A.; Mitchell, T.A.; Kiley, J.L.; Wellington, T.; Britton, G.W.; Cancio, L.C. Diagnosis and Management of Invasive Fungal Wound Infections in Burn Patients. *Eur. Burn J.* **2021**, *2*, 168–183. [[CrossRef](#)]
87. Struck, M.F.; Gille, J. Fungal Infections in Burns: A Comprehensive Review. *Ann. Burn. Fire Disasters* **2013**, *26*, 147–153.
88. Szunerits, S.; Boukherroub, R. Antibacterial Activity of Graphene-Based Materials. *J. Mater. Chem. B* **2016**, *4*, 6892–6912. [[CrossRef](#)]
89. Jira, J.; Rezek, B.; Kriha, V.; Artemenko, A.; Matolínová, I.; Skakalova, V.; Stenclova, P.; Kromka, A. Inhibition of *E. coli* Growth by Nanodiamond and Graphene Oxide Enhanced by Luria-Bertani Medium. *Nanomaterials* **2018**, *8*, 140. [[CrossRef](#)] [[PubMed](#)]
90. Nunes-Pereira, J.; Costa, P.; Fernandes, L.; Carvalho, E.O.; Fernandes, M.M.; Carabineiro, S.A.C.; Buijnsters, J.G.; Tubio, C.R.; Lanceros-Mendez, S. Antimicrobial and Antibiofilm Properties of Fluorinated Polymers with Embedded Functionalized Nanodiamonds. *ACS Appl. Polym. Mater.* **2020**, *2*, 5014–5024. [[CrossRef](#)]
91. Kumar, P.; Huo, P.; Zhang, R.; Liu, B. Antibacterial Properties of Graphene-Based Nanomaterials. *Nanomaterials* **2019**, *9*, 737. [[CrossRef](#)]
92. Hochvaldová, L.; Panáček, D.; Válková, L.; Pucek, R.; Kohlová, V.; Večeřová, R.; Kolář, M.; Kvítek, L.; Panáček, A. Restoration of Antibacterial Activity of Inactive Antibiotics via Combined Treatment with a Cyanographene/Ag Nanohybrid. *Sci. Rep.* **2022**, *12*, 5222. [[CrossRef](#)]
93. Vi, T.T.T.; Kumar, S.R.; Pang, J.-H.S.; Liu, Y.-K.; Chen, D.W.; Lue, S.J. Synergistic Antibacterial Activity of Silver-Loaded Graphene Oxide towards *Staphylococcus aureus* and *Escherichia coli*. *Nanomaterials* **2020**, *10*, 366. [[CrossRef](#)]
94. Wehling, J.; Dringen, R.; Zare, R.N.; Maas, M.; Rezwan, K. Bactericidal Activity of Partially Oxidized Nanodiamonds. *ACS Nano* **2014**, *8*, 6475–6483. [[CrossRef](#)]
95. Turcheniuk, V.; Turcheniuk, K.; Bouckaert, J.; Barras, A.; Dumych, T.; Bilyy, R.; Zaitsev, V.; Siriwardena, A.; Wang, Q.; Boukherroub, R.; et al. Affinity of Glycan-Modified Nanodiamonds towards Lectins and Uropathogenic *Escherichia coli*. *ChemNanoMat* **2016**, *2*, 307–314. [[CrossRef](#)]
96. Iyer, J.K.; Dickey, A.; Rouhani, P.; Kaul, A.; Govindaraju, N.; Singh, R.N.; Kaul, R. Nanodiamonds Facilitate Killing of Intracellular Uropathogenic *E. coli* in an in Vitro Model of Urinary Tract Infection Pathogenesis. *PLoS ONE* **2018**, *13*, e0191020. [[CrossRef](#)] [[PubMed](#)]
97. Panáček, D.; Hochvaldová, L.; Bakandritsos, A.; Malina, T.; Langer, M.; Belza, J.; Martincová, J.; Večeřová, R.; Lazar, P.; Poláková, K.; et al. Silver Covalently Bound to Cyanographene Overcomes Bacterial Resistance to Silver Nanoparticles and Antibiotics. *Adv. Sci.* **2021**, *8*, 2003090. [[CrossRef](#)] [[PubMed](#)]
98. Lin, Y.-C.; Perevedentseva, E.; Tsai, L.-W.; Wu, K.-T.; Cheng, C.-L. Nanodiamond for Intracellular Imaging in the Microorganisms in Vivo. *J. Biophotonics* **2012**, *5*, 838–847. [[CrossRef](#)] [[PubMed](#)]
99. Gutiérrez, J.M.B.; Conceição, K.; de Andrade, V.M.; Trava-Airoldi, V.J.; Capote, G. High Antibacterial Properties of DLC Film Doped with Nanodiamond. *Surf. Coat. Technol.* **2019**, *375*, 395–401. [[CrossRef](#)]